Manifestation of asymmetric manganite-ruthenate interfaces

Haoming Ling,[1,2] Xin Du,[3,4] Zhixiong Deng,[5] Kai Hu,[1] Qiangtao Sui,[1] Zixin Fan,[1,2] Lingyuan Kong,[1] Dingyi Li,[1,2] Shaojie Tai,[1,2] Wei Li,[1] Yan Liang,[1] Pan Chen,[1] Kai Liu,[3,4] Zhaoliang Liao,[5] Meng Meng,[1,2] Xiaoran Liu,[1,2] Zhen Wang,[6] and Jiandi Zhang[1,2,*]

[1]*Beijing National Laboratory for Condensed Matter Physics, Institute of Physics, Chinese Academy of Sciences, Beijing 100190, China*
[2]*College of Physics, University of Chinese Academy of Sciences, Beijing 100190, China*
[3]*School of Physics and Beijing Key Laboratory of Opto-electronic Functional Materials & Micro-nano Devices, Renmin University of China, Beijing 100872, China*
[4]*Key Laboratory of Quantum State Construction and Manipulation (Ministry of Education), Renmin University of China, Beijing 100872, China*
[5]*School of National Synchrotron Radiation Laboratory, University of Science and Technology of China, Hefei 230026, China*
[6]*Department of Physics, University of Science and Technology of China, Hefei, Anhui 230026, China*

(Received 10 February 2026; revised 23 April 2026; accepted 1 June 2026; published 6 July 2026)

Interfacial magnetism in complex oxide heterostructures underlies both fundamental many-body physics and advanced spintronic applications. Here we report a pronounced stacking-order dependence of magnetic coupling in $La_{0.78}Ca_{0.22}MnO_3/SrRuO_3$ (LCMO/SRO) bilayers. While Ru–O–Mn superexchange drives antiparallel spin alignment between interfacial Ru and Mn moments, macroscopic antiferromagnetic correlations emerge only within a proper thickness ratio range, consistent with first-principles calculations. Ferromagnetic enhancement—manifested as a significant increase in Curie temperature (T_C)—occurs exclusively when LCMO is grown atop SRO, vanishing in the inverse stack. Atomically resolved structural analysis attributes this unidirectional phenomenon to suppressed Jahn-Teller distortions and preferential in-plane orientation of the LCMO crystallographic c axis in the LCMO grown on SRO configuration, which together strengthen double-exchange interactions. Control experiments rule out interfacial charge transfer and Sr interdiffusion as primary mechanisms. These findings establish that stacking-sequence–induced structural asymmetry serves as a dominant control parameter for interfacial ferromagnetism, offering a deterministic route to engineer correlated oxide heterostructures.

DOI: 10.1103/mxfx-fg4f

I. INTRODUCTION

The interfaces between crystalline materials break symmetry, reduce dimensionality, and create tailored atomic interactions, giving rise to distinct quantum states not found in the bulk. By modifying lattice structures, electronic bands, and magnetic orders, these interfaces enable emergent phenomena like superconductivity, two-dimensional electron gases, and novel magnetic phases [1–3]. A prime example is the engineering of magnetic coupling through heterostructure design. In synthetic antiferromagnets—ferromagnetic layers separated by a nonmagnetic spacer—the Ruderman-Kittel-Kasuya-Yosida (RKKY) interaction mediates interlayer coupling [4], a mechanism central to giant magnetoresistance (GMR) devices.

Recent advances in epitaxial synthesis now enable the creation of atomically sharp interfaces in complex oxide heterostructures [1–3,5]. This precision allows the tailoring of exchange interactions at the atomic scale and the emergence of novel magnetic states, mediated by interfacial charge transfer, structural coupling, and orbital reconstruction. However, compared to conventional GMR materials, these oxide interfaces exhibit far greater complexity in their structure, chemistry, and exchange mechanisms, posing a fundamental challenge to a complete understanding of their interfacial magnetism.

In oxide heterostructures, perovskite ruthenate $SrRuO_3$ (SRO) and manganite $La_{1-x}Ca_xMnO_3$ serve as extensively studied prototypical systems. In bulk form, both exhibit ferromagnetic metallic ground states within orthorhombic lattice structures. $La_{1-x}Ca_xMnO_3$ ($0.175 < x < 0.5$) displays a strongly doping-dependent Curie temperature (T_C), which peaks at approximately 265 K for $x \approx 1/3$, with an in-plane magnetic easy axis [6–9]. By contrast, SRO has a ferromagnetic ground state with $T_C \sim 160$ K and magnetization oriented primarily along the c axis. This configuration makes SRO a magnetically hard material, distinct from the softer manganites [10–15].

In manganite-ruthenate bilayers, the properties diverge significantly from those of the bulk constituents. The layers themselves remain ferromagnetic, yet they couple antiparallel across the interface [7,16–23]. This interfacial magnetism can be modified by epitaxial strain, which alters electron orbital occupancy. According to the Goodenough-Kanamori-Anderson (GKA) rules, these orbital changes directly

*Contact author: jiandiz@iphy.ac.cn

influence whether ferromagnetic or antiferromagnetic interactions dominate [18–25]. While enhancements of the manganite's T_C have been ascribed to charge transfer or Sr interdiffusion [16,26–29], the fundamental mechanisms at the interface remain unresolved. The precise origin of the spin-antiparallel coupling and the pathway for T_C enhancement are still debated, with the potential roles of strain, lattice distortions, and orbital reconstructions yet to be fully clarified.

In this work, we employ underdoped $La_{0.78}Ca_{0.22}MnO_3/SrRuO_3$ (LCMO/SRO) heterostructures as a model system to investigate interfacial magnetic interactions in correlated oxides. By systematically varying the stacking sequence and layer thickness, we find that antiparallel spin coupling across the interface—mediated by superexchange along interfacial Mn–O–Ru bonds—is robust across all configurations, as confirmed by first-principles calculations. In stark contrast, ferromagnetic enhancement manifested as a significant T_C increase occurs exclusively when LCMO is grown atop SRO, revealing pronounced stacking-sequence asymmetry. This unidirectional enhancement originates from suppressed Jahn-Teller distortions and preferential in-plane orientation of the LCMO crystallographic c axis in the LCMO/SRO configuration, which collectively strengthen double-exchange interactions within the manganite layer. Control experiments using ultrathin $SrTiO_3$ (STO) spacer layers, combined with layer-resolved spectroscopic measurements, exclude Mn-valence modification and Sr interdiffusion as dominant mechanisms. These findings establish that interface geometry and stacking-sequence–induced structural asymmetry, rather than chemical reconstruction alone, constitute the primary determinants of emergent magnetism in manganite-ruthenate heterostructures.

II. EXPERIMENTAL DETAILS

Thin films and heterostructures in this study were fabricated via pulsed laser deposition (PLD) in an ultrahigh vacuum chamber with a base pressure of 5×10^{-8} mbar, using a 248 nm KrF excimer laser (Coherent). Before deposition, (001)-oriented STO substrates were preannealed at 1350 °C for one hour under a vacuum of 5×10^{-5} mbar to achieve a uniform TiO_2-terminated surface. Prior to growth, substrates were further heated to 650 °C in 200 mbar O_2 for 30 min to reduce oxygen vacancies. LCMO and SRO layers were deposited at 0.15 mbar with 5% O_3 and 0.1 mbar with 1% O_3, respectively. A laser fluence of $\sim$2 J/cm^2 and repetition rate of 3 Hz were used for all depositions. The crystalline quality of the films was confirmed by thin-film x-ray diffraction, as shown in Fig. S1 [Supplemental Material (SM) [30]].

Magnetic characterization was performed using a Magnetic Property Measurement System (MPMS, Quantum Design). Measurements were conducted from 5 to 300 K with an applied magnetic field oriented along either the in-plane [100] or out-of-plane [001] directions. Temperature-dependent magnetization (M–T) curves were acquired on warming under a 0.01 T field after field cooling in a 1 T magnetic field. The diamagnetic background from the substrate was subtracted from all data. Representative magnetization data are presented in Figs. S2–S3 of SM [30].

Scanning transmission electron microscopy (STEM) and electron energy loss spectroscopy (EELS) measurements were conducted on a double aberration-corrected JEOL GrandARM microscope operating at 300 kV, equipped with a Gatan K3 direct electron detector. Cross-sectional samples were prepared using focused ion beam (FIB) milling with Ga^+ ions. High-angle annular dark-field (HAADF) images were acquired with an inner collection angle of 68 mrad and an outer angle of 280 mrad. Lattice parameters and A-site displacements were quantified by fitting atomic column positions in the HAADF images using two-dimensional Gaussian peak profiles.

For atomic-resolution EELS, the electron probe was optimized with a diameter of 0.7 Å, a convergence semiangle of 11 mrad, and a collection semiangle of 100 mrad. Spectrum imaging was performed across the interface using a step size of 0.08 Å and a dwell time of 0.001 s per pixel, recorded with the K3 detector. Background was subtracted using a power-law model and plural scattering contributions were removed via Fourier deconvolution. Elemental concentrations were determined from EELS intensity profiles after calibration with reference standards. To track changes in the oxidation state, the $L_{2,3}$ edge intensity ratios were analyzed across the films.

X-ray absorption spectroscopy (XAS) measurements were conducted in total-electron-yield (TEY) detection mode at Beamline BL08U2A of the Shanghai Synchrotron Radiation Facility (SSRF). Spectra were acquired at room temperature under ultrahigh vacuum ($<2 \times 10^{-8}$ Torr) with incident x ray along the surface normal direction. The energy resolution was set to 0.1 eV for both the Mn $L_{2,3}$ and O K edges, with a photocurrent sensitivity of 10 pA. To enhance signal-to-noise ratios, each spectrum represents an average of 20 measurement cycles. Mn $L_{2,3}$ edge spectra were normalized to the L_3 peak maximum, while O K-edge spectra were normalized to the hybridization peak arising from La5d/Ca3d−O2p orbital mixing.

III. RESULTS AND DISCUSSION

A. Interface structural asymmetry

We first examine the structural difference introduced by the stacking sequence. Figures 1(a)–1(d) present atomic-resolution STEM-HAADF images alongside schematics of the interfaces for the LCMO/SRO and SRO/LCMO heterostructures (where A/B denotes A grown on B, hereafter). These images confirm high-quality epitaxial growth and reveal a distinct asymmetry between the two stackings.

The interfacial terminations differ fundamentally: in the LCMO/SRO heterostructure, the SRO surface is RuO_2 terminated and bonds to a polar (La/Ca)O layer from LCMO [Fig. 1(b)]. Conversely, in the SRO/LCMO stacking, the LCMO surface is MnO_2 terminated and bonds to a nonpolar SrO layer from SRO [Fig. 1(d)]. The polar (La/Ca)O layer, with a nominal valence of $(1-x)^+$, possesses an intrinsic charge polarity known to drive interfacial charge transfer [17,29,31–35]. The SrO layer, in contrast, is charge neutral. This stark contrast in termination chemistry creates a significant structural and electronic asymmetry at the interface.

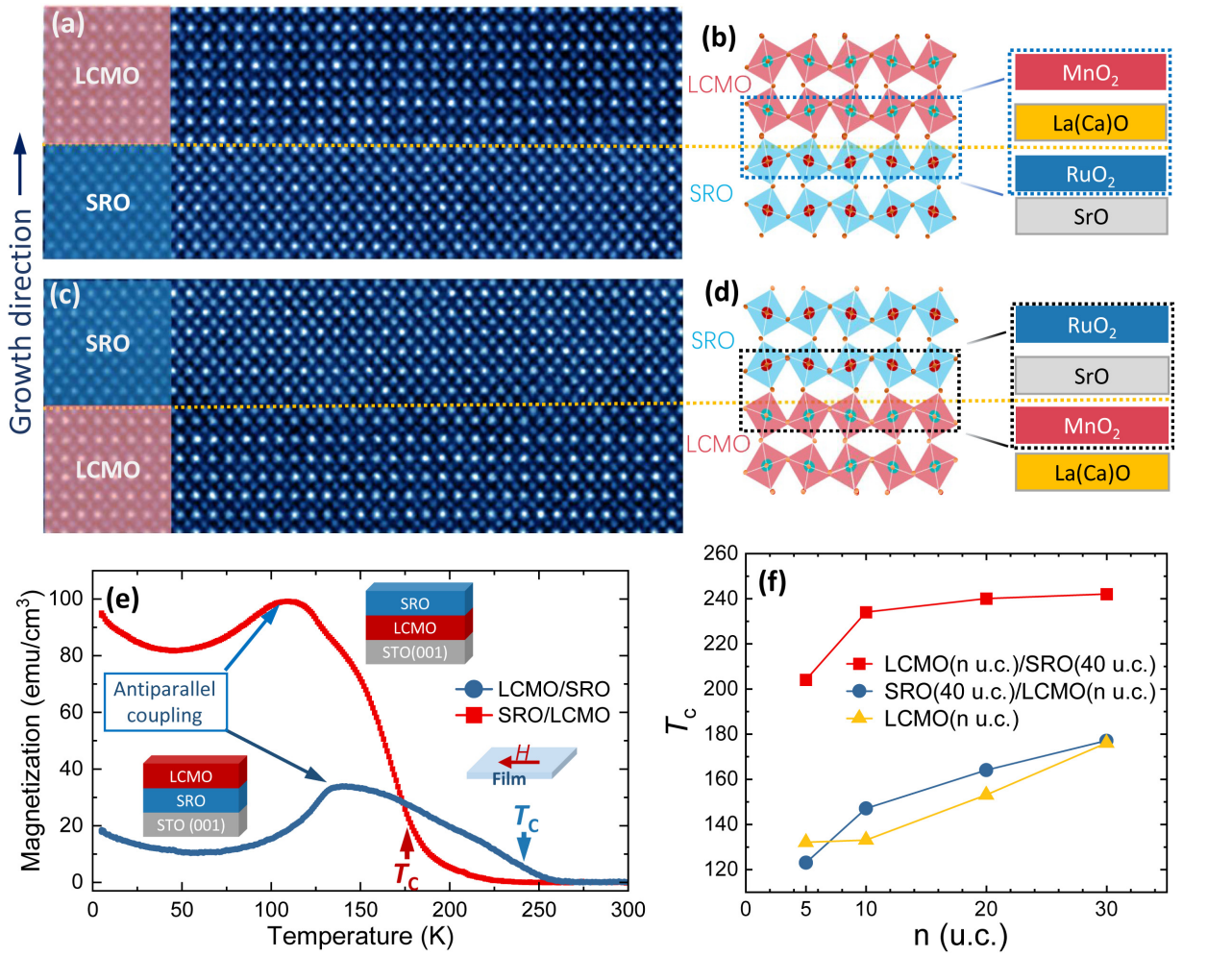

FIG. 1. Structural and magnetic asymmetry induced by stacking sequence. HAADF-STEM images and corresponding schematics of the interfaces in the (a), (b) LCMO (20 u.c.) grown on a bottom SRO layer (40 u.c.) and (c), (d) LCMO (20 u.c.) capped by an SRO capping layer (40 u.c.), revealing distinct interface configurations associated with the two stacking geometries. The schematics in (b) and (d) illustrate the stacking sequences and the resulting asymmetric magnetic boundary conditions imposed on the LCMO layer by the bottom and capping SRO layers. (e) Temperature-dependent in-plane magnetization of the LCMO/SRO and reversed SRO/LCMO stacking heterostructures shown in (a) and (c), indicating spin-antiparallel magnetic coupling between LCMO and SRO. The Curie temperatures (T_C) are determined from extrema in dM/dT and marked by arrows. (f) LCMO thickness dependence of T_C in heterostructures with a bottom SRO layer and an SRO capping layer, together with that of a single-layer LCMO film for comparison. The SRO thickness is fixed at 40 u.c.

B. Interface antiparallel coupling

Figure 1(e) presents the in-plane magnetization $M_{\parallel}(T)$ as a function of temperature for two prototype heterostructures: LCMO(20 u.c.)/SRO(40 u.c.) and SRO(40 u.c.)/LCMO(20 u.c.), both showing nonmonotonic variations. By lowering temperature, $M_{\parallel}(T)$ shows a $T_C \sim 240$ K for LCMO/SRO and ~160 K for SRO/LCMO, respectively. This behavior is primarily attributed to the in-plane ferromagnetic contribution from the LCMO layer. As shown in Fig. S2, and consistent with previous reports, LCMO in our heterostructure exhibits strong in-plane magnetic anisotropy, whereas SRO favors out-of-plane magnetization. Furthermore, the magnetic moment of Mn is substantially larger than that of Ru [36–38]. Consequently, under an in-plane magnetic field, the measured magnetic response is dominated by the LCMO layer. Then, both samples exhibit a sudden reduction in $M_{\parallel}(T)$ when further cooling down across $T_{AP} \sim 138$ K for LCMO/SRO and ~110 K for the reversed stacking one. This reduction signals an antiparallel magnetic coupling at the interface when SRO starts to form its out-of-plane canted FM order. This interfacial antiparallel spin coupling persists in heterostructures with thicker LCMO layers [see Figs. S3(a) and S3(b) in the SM [30]].

This interfacial magnetic state arises primarily from the strong local moments of LCMO, which force the interfacial SRO spins into an antiparallel alignment [36]. Consequently, while the bulk regions of both LCMO and SRO retain their ferromagnetic order, the interface hosts a localized antiparallel spin configuration. The competition between intralayer ferromagnetism and this interlayer antiparallel coupling results in the observed nonmonotonic evolution of the net in-plane magnetization with temperature.

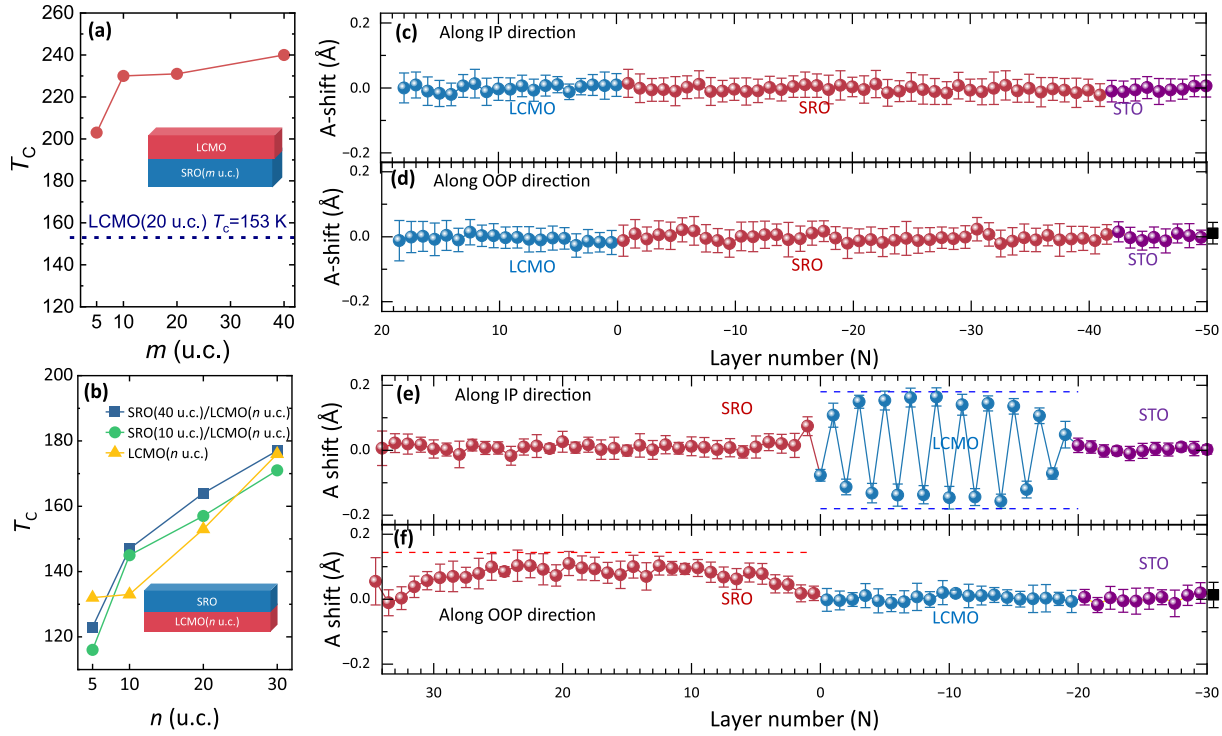

FIG. 2. Stacking-sequence–dependent structural asymmetry and its impact on T_C. (a) T_C of LCMO (20 u.c.) films grown on bottom SRO layers with varying thicknesses (5, 10, 20, and 40 u.c.), compared with a single-layer LCMO (20 u.c.) film (yellow dashed line). (b) T_C of LCMO films with varying thicknesses (5, 10, 20, and 30 u.c.) capped by SRO layers of different thicknesses (10 and 40 u.c.), compared with single-layer LCMO films of corresponding thicknesses. (c), (d) In-plane and (e), (f) out-of-plane A-site displacement profiles for the LCMO/SRO and the reversed SRO/LCMO stacking heterostructure, respectively, extracted from a [100]-zone HAADF-STEM image.

C. Stacking-order–dependent ferromagnetic (FM) enhancement

The Curie temperature (T_C) of LCMO layers exhibits a pronounced dependence on the stacking sequence in LCMO/SRO heterostructures. To isolate this interface-driven effect, we fabricated two distinct series: LCMO(n u.c.) grown on SRO(40 u.c.) layer and SRO(40 u.c.) grown on LCMO(n u.c.) layers, systematically varying the LCMO thickness n from 5 to 30 unit cells. In-plane magnetization measurements reveal that T_C rises sharply with increasing n from 5 to 20 u.c. before saturating for thicker layers in both configurations [Fig. 1(f); raw data in Figs. S3(a) and S3(b)]. However, the *magnitude* of enhancement is strongly governed by stacking order. Heterostructures with SRO capping layers show only a moderate increase over monolithic LCMO films, whereas those with bottom SRO layers yield a substantial enhancement of ∼60–80 K across all thicknesses, culminating in a saturated T_C of ∼240 K.

Since the in-plane magnetic signal is dominated by LCMO (SRO magnetizes primarily out of plane), these results demonstrate that the adjacent SRO layer profoundly modifies LCMO ferromagnetism in a direction-dependent manner. The minimal enhancement in the ultrathin LCMO(5 u.c.)/SRO sample aligns with magnetic "*dead layer*" behavior, where carrier depletion suppresses the double-exchange mechanism [39–44]. Conversely, the robust, thickness-saturated enhancement to ∼240 K in thicker LCMO/SRO heterostructures indicates a fundamental limit to the interfacial mechanism driving the T_C increase.

This stacking asymmetry persists when varying the SRO thickness. As shown in Figs. 2(a) and 2(b), T_C increases monotonically with the bottom SRO layer thickness for LCMO(20 u.c.), consistently exceeding that of single-layer LCMO. In contrast, increasing the SRO capping layer thickness produces only weak effects across different LCMO thicknesses. Notably, this geometric dependence occurs despite robust interfacial spin-antiparallel coupling in all configurations (Fig. S3), demonstrating that T_C enhancement is governed primarily by heterostructure geometry rather than interfacial magnetic coupling alone.

Quantitative structural analysis identifies the origin of this asymmetry in distinct octahedral distortion profiles. In LCMO/SRO heterostructures, layer-resolved A-site displacements remain close to zero throughout the film thickness, indicating a uniform suppression of rotational distortions within the MnO_6 octahedra [Figs. 2(c) and 2(d)]. This renders the LCMO layer more cubic-like, promoting ferromagnetism via enhanced double-exchange interactions. Conversely, SRO/LCMO heterostructures exhibit pronounced layer-by-layer oscillations in A-site zigzag displacements coupled with nonuniform out-of-plane shifts [Figs. 2(e) and 2(f)]. These distortions drive the LCMO toward a more orthorhombic geometry, suppressing double-exchange interactions and consequently weakening ferromagnetic order.

Beyond octahedral distortions, the stacking sequence determines the crystallographic orientation of LCMO, which acts cooperatively with the octahedral geometry to reinforce

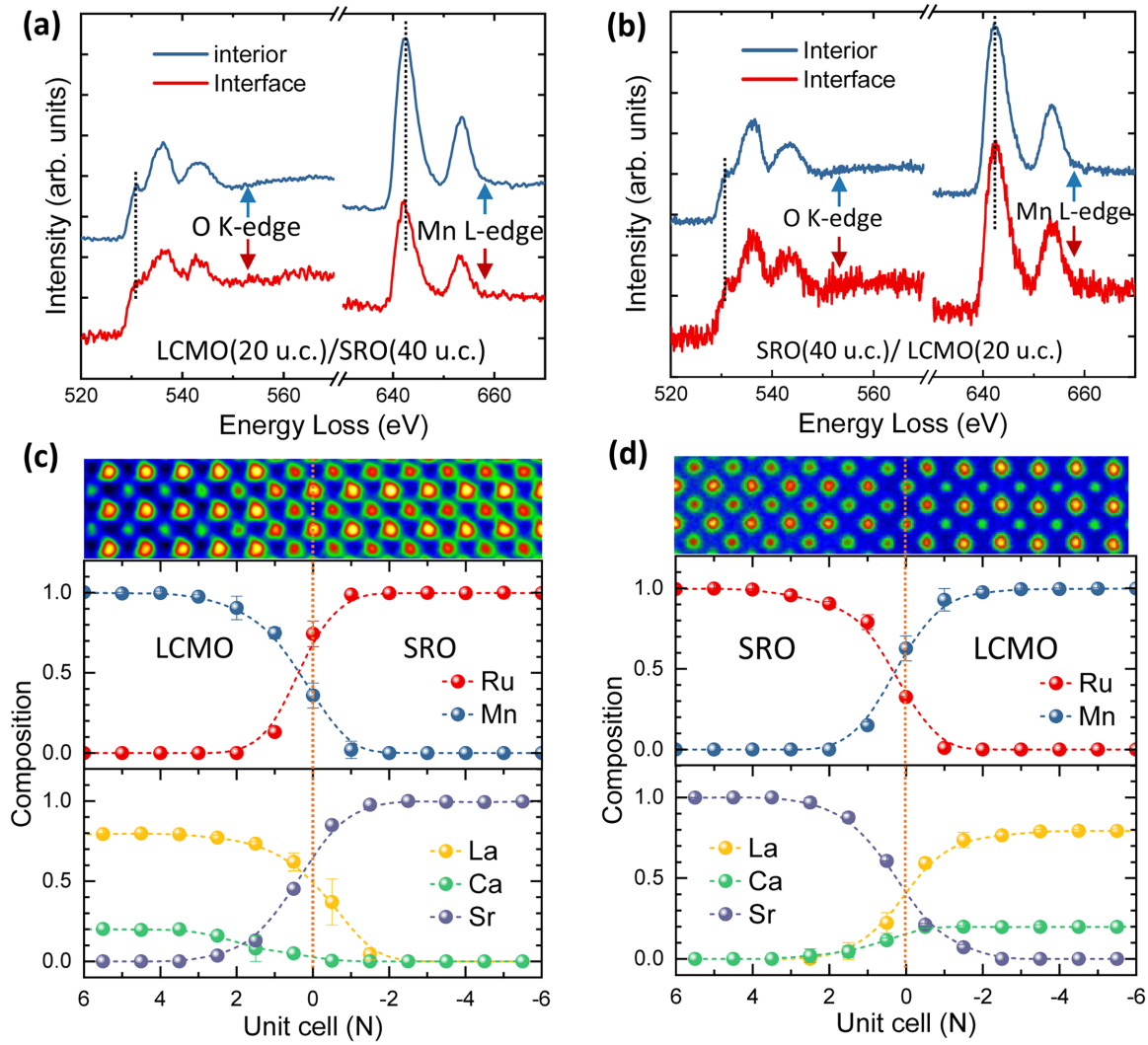

FIG. 3. Interface chemical composition and Mn valence analysis. (a), (b) Background-subtracted EELS spectra acquired from the interior and interfacial regions of the LCMO/SRO and SRO/LCMO heterostructures, respectively. HAADF-STEM images of the (c) LCMO(20 u.c.)/SRO(40 u.c.) and (d) SRO(40 u.c.)/LCMO(20 u.c.) heterostructures with corresponding elemental concentration profiles of Sr, Ca, La, Ru, and Mn, respectively. The spectra are averaged over multiple regions within each film to improve statistical reliability.

the asymmetric magnetic response. In LCMO/SRO, the LCMO *c* axis lies preferentially in-plane and aligns coherently with the underlying SRO layer, whereas in SRO/LCMO—or when STO interlayers are introduced—the *c* axis orients predominantly out of plane (Figs. S5 and S6). The combination of reduced octahedral distortion and favorable in-plane lattice orientation in LCMO/SRO yields the enhanced T_C, whereas the stronger distortions and unfavorable out-of-plane orientation in SRO/LCMO coincide with suppressed ferromagnetism.

These findings establish that stacking-sequence–induced structural differences—governed primarily by the degree of octahedral distortions and modulated by lattice orientation—constitute the origin of the asymmetric ferromagnetic enhancement. The heterostructure geometry thus dictates whether the interfacial environment supports robust ferromagnetism in the LCMO layer. This structural interpretation is corroborated by XAS measurements (Fig. S7): relative to pure LCMO films, the LCMO layer in LCMO/SRO heterostructures exhibits an ∼0.3 eV shift in the Mn *L* edge and distinct modifications to the O *K*-edge prepeak, signaling changes in the Mn chemical environment and covalency [39,45–47]. Direct measurement of the buried LCMO layer in SRO/LCMO was precluded by the thick capping layer; however, its structural characteristics are expected to mirror those of pure LCMO grown on STO. These spectroscopic observations remain consistent with the proposed structural asymmetry between the two stacking configurations.

D. Relative thickness effect

Irrespective of stacking order, macroscopic antiferromagnetism emerges only when the magnetic moments of the LCMO and SRO layers are comparable—that is, within a specific range of thickness ratios [Figs. S3(a) and S3(b)]. This compensation behavior indicates that the observed macroscopic AFM response arises from interfacial spin-antiparallel coupling between the two ferromagnetic layers, rather than from an intrinsic antiferromagnetic phase localized at the

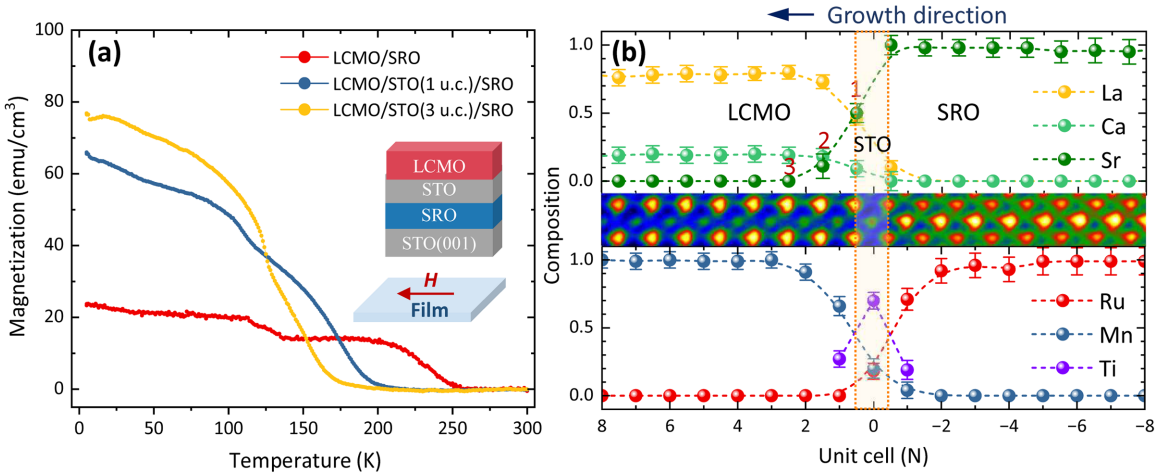

FIG. 4. Sr/Ca interdiffusion effect in magnetic enhancement. (a) Temperature-dependent magnetization of LCMO(10 u.c.)/STO/bottom SRO layer (40 u.c.) heterostructures with different STO thicknesses, indicating that Sr diffusion alone cannot account for the magnetic enhancement. (b) Elemental concentration profiles of La, Sr, Ca, Ru, and Mn in LCMO(10 u.c.)/STO(1 u.c.)/bottom SRO layer (40 u.c.), showing Sr diffusion extending over ∼3 u.c. into the LCMO layer.

interface. When the magnetization of LCMO is substantially weaker than that of SRO, the LCMO aligns ferromagnetically with SRO via magnetic proximity, yielding a net FM response. Conversely, when LCMO magnetization dominates, it dictates the net alignment, again resulting in a ferromagnetic state. Only when the layer magnetizations are balanced does the spin-antiparallel coupling at the interface manifest macroscopically.

To verify this thickness-ratio dependence, we reduced the SRO thickness to 10 u.c. while systematically varying the LCMO thickness (5, 10, 20, and 30 u.c.) in SRO/LCMO heterostructures. As shown in Fig. S3(c), this reduction shifts the balance point: spin-antiparallel coupling becomes evident even at LCMO(5 u.c.) (where moments are now comparable), whereas macroscopic antiferromagnetism disappears once LCMO reaches 30 u.c. (where LCMO magnetization dominates).

To determine the microscopic origin of this coupling, we inserted thin STO buffer layers (1 and 3 u.c.) between SRO(40 u.c.) and LCMO(10 u.c.). As shown in Fig. S3(d), buffered heterostructures exhibit the same T_C as LCMO single layers [Fig. S2(a)] and show no detectable AFM signal—unlike the unbuffered control. This demonstrates that the spin-antiparallel coupling requires direct exchange between Ru and Mn moments across the interface. Without the STO spacer, interfacial Ru and Mn spins couple antiparallel while the interior of each layer maintains FM order. Inserting Ti-containing STO disrupts the direct Ru–O–Mn exchange pathway, eliminating the antiparallel alignment and restoring independent ferromagnetic behavior. Thus the macroscopic AFM response originates from interfacial exchange coupling between the ferromagnetic layers, mediated by Ru–O–Mn bonds, rather than from the formation of a distinct antiferromagnetic phase at the interface.

E. Ruling out charge transfer and Sr diffusion

To verify that the observed T_C enhancement originates from structural modifications rather than electronic or chemical intermixing effects, we examined two alternative mechanisms proposed in the literature: interfacial charge transfer [17] and Sr/Ca interdiffusion [29].

First, electron energy-loss spectroscopy (EELS) of the Mn ($L_{2,3}$) and O (K) edges reveals no significant change in Mn valence state between interfacial and interior regions of the LCMO layer for either stacking sequence [Figs. 3(a) and 3(b)]. Although minor spectral variations are detectable, the absence of a systematic valence shift indicates that charge transfer—potentially expected at polar discontinuities—does not dominate the stacking-dependent magnetic response.

We next investigated cation interdiffusion. B-site (Ru/Mn) intermixing is confined to within ∼2 u.c. of the interface in both configurations [Figs. 3(c) and 3(d)] and thus too limited to account for the pronounced magnetic asymmetry. A-site analysis reveals almost the same Sr/Ca interdiffusion: the exchange extends approximately 3 u.c. into the LCMO layer in LCMO/SRO heterostructures [Fig. 3(c)] while ∼2 u.c. in SRO/LCMO [Fig. 3(d)].

To determine whether this differential Sr/Ca interdiffusion drives the T_C enhancement, we inserted 1 u.c. and 3 u.c. STO buffer layers into LCMO(10 u.c.)/SRO(40 u.c.) heterostructures. Magnetic measurements [Fig. 4(a)] show that increasing STO thickness progressively suppresses the T_C enhancement. Crucially, however, atomic-layer-resolved compositional analysis indicates that Sr/Ca interdiffusion still extends ∼3 u.c. into the LCMO layer even with the STO spacer [Fig. 4(b)]. Since the T_C enhancement diminishes while the Sr diffusion depth persists, we conclude that Sr/Ca interdiffusion occurs but is not the primary factor behind the asymmetric ferromagnetic enhancement.

F. First principles calculations

To elucidate the interfacial magnetic coupling, we performed density functional theory (DFT) calculations on the LCMO/SRO heterostructure (see SM [30] for computational details). The model consists of a 17-layer slab (32 formula units) of $(La_{0.75}Ca_{0.25})MnO_3$/SRO capped with an

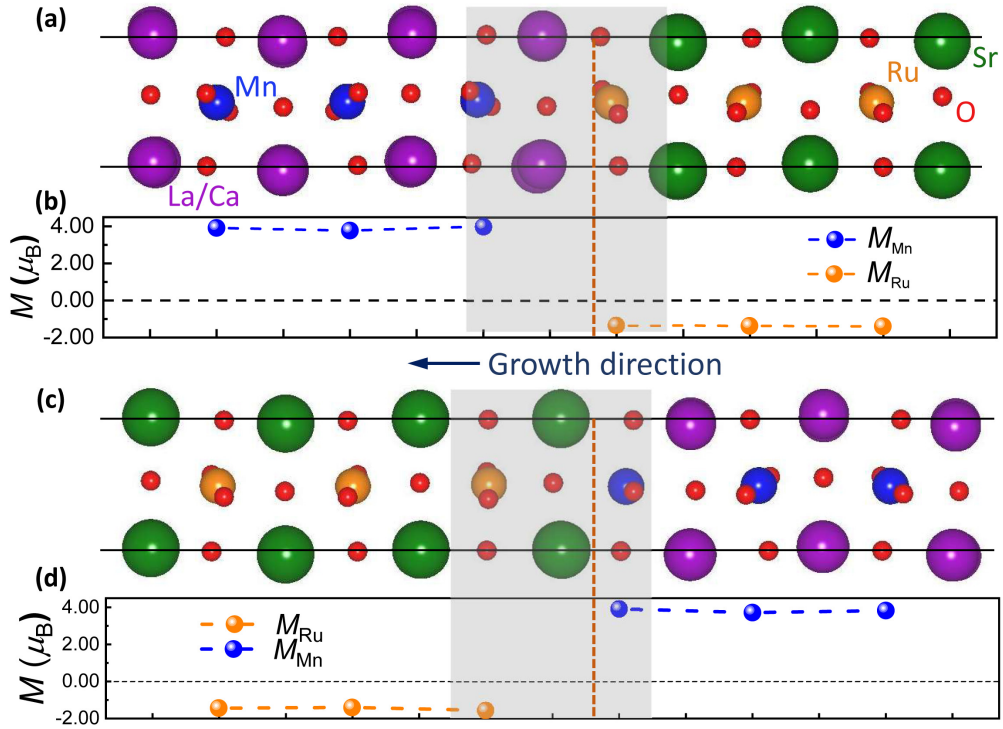

FIG. 5. Microscopic origin of interfacial antiferromagnetic coupling. (a), (b) Schematic structure and layer-resolved local magnetic moments for the LCMO/SRO stacking, showing antiparallel alignment between Mn (blue) and Ru (orange) magnetic moments at the interface. (c), (d) Corresponding schematic structure and layer-resolved magnetic moments for the reversed SRO/LCMO stacking.

$(La_{0.75}Ca_{0.25})_8O_8$ layer to ensure convergence and maintain MnO_6 octahedral coordination. This heterostructure contains an MnO_2–(La/Ca)O–RuO_2 interface [Fig. S10(a)], with electronic and magnetic properties analyzed for the central layers (3–15) near this interface [Fig. 5(a)].

We compared spin-parallel and spin-antiparallel interfacial configurations to determine the magnetic ground state (Fig. S11). The calculations reveal that the energetically most favorable configuration exhibits spin-parallel coupling within both LCMO and SRO layers, but spin-antiparallel coupling across the interface (Table I), consistent with superexchange between Mn and Ru spins via bridging oxygen atoms. Local magnetic moments are calculated to be $\approx 3.9\mu_B$ for Mn and $\approx 1.4\mu_B$ for Ru [Fig. 5(b)]. Notably, interfacial Ru atoms show a significant moment reduction ($\Delta M \approx 0.07\mu_B$), whereas interfacial Mn moments remain largely unaffected—results consistent with prior studies on LSMO/SRO superlattices.

For comparison, we also examined the inverse SRO/LCMO heterostructure with a RuO_2–SrO–MnO_2 interface [Figs. 5(c) and 5(d)]. As expected, the interfacial spin-antiparallel-coupled configuration remains the most stable magnetic ground state, consistent with our experimental results.

TABLE I. Total energy differences ($\Delta E = E_{AFM} - E_{FM}$) for the ferromagnetic (FM) and antiferromagnetic (AFM) couplings across the interface for LCMO/SRO and SRO/LCMO heterostructures obtained from DFT calculations.

Heterostructure	ΔE (meV)
LCMO/SRO (LCMO on SRO)	−132.7
SRO/LCMO (SRO on LCMO)	−70.1

IV. SUMMARY

In conclusion, we demonstrate that both interfacial antiferromagnetism and the macroscopic T_C enhancement in LCMO/SRO heterostructures originate from interface interactions, albeit via distinct mechanisms. Interfacial spin-antiparallel coupling between Ru and Mn moments arises from superexchange through Mn–O–Ru bonds, producing local antiferromagnetism that persists regardless of stacking order. Conversely, pronounced T_C enhancement is exclusive to LCMO/SRO heterostructures, where stacking-sequence–induced structural asymmetry—specifically, suppressed octahedral distortions and favorable in-plane c-axis orientation—strengthens ferromagnetic exchange. Control experiments using layer-resolved EELS and ultrathin STO interlayers confirm that interface charge transfer and Sr interdiffusion, though potentially present, are not the dominant factors in either phenomenon.

ACKNOWLEDGMENTS

This work was supported by the National Key Research and Development Program of China (Grants No. 2022YFA1403000 and No. 2022YFA1403103) and the National Natural Science Foundation of China (Grants No. 12250710675 and No. U23A20366). X-ray absorption spectroscopy measurements were performed at beamline

BL08U2A of the Shanghai Synchrotron Radiation Facility (SSRF). Computational resources have been provided by the Physical Laboratory of High Performance Computing at Renmin University of China and the Beijing Super Cloud Computing Center.

DATA AVAILABILITY

The data that support the findings of this article are not publicly available. The data are available from the authors upon reasonable request.

[1] H. Y. Hwang, Y. Iwasa, M. Kawasaki, B. Keimer, N. Nagaosa, and Y. Tokura, Emergent phenomena at oxide interfaces, Nat. Mater. **11**, 103 (2012).

[2] J. Chakhalian, J. W. Freeland, A. J. Millis, C. Panagopoulos, and J. M. Rondinelli, *Colloquium*: Emergent properties in plane view: Strong correlations at oxide interfaces, Rev. Mod. Phys. **86**, 1189 (2014).

[3] C. Ahn, A. Cavalleri, A. Georges, S. Ismail-Beigi, A. J. Millis, and J.-M. Triscone, Designing and controlling the properties of transition metal oxide quantum materials, Nat. Mater. **20**, 1462 (2021).

[4] R. A. Duine, K.-J. Lee, S. S. P. Parkin, and M. D. Stiles, Synthetic antiferromagnetic spintronics, Nat. Phys. **14**, 217 (2018).

[5] A. Bhattacharya and S. J. May, Magnetic oxide heterostructures, Annu. Rev. Mater. Res. **44**, 65 (2014).

[6] A. Moreo, S. Yunoki, and E. Dagotto, Phase separation scenario for manganese oxides and related materials, Science **283**, 2034 (1999).

[7] B. Chen *et al.*, All-oxide-based synthetic antiferromagnets exhibiting layer-resolved magnetization reversal, Science **357**, 191 (2017).

[8] R. Shreekala *et al.*, Ferromagnetism at room temperature in $La_{0.8}Ca_{0.2}MnO_3$ thin films, Appl. Phys. Lett. **74**, 1886 (1999).

[9] R. Skini, M. Khlifi, E. Dhahri, and E. K. Hlil, Magnetocaloric-transport properties correlation in $La_{0.8}Ca_{0.2}MnO_3$-doped manganites, J. Supercond. Nov. Magn. **30**, 3091 (2017).

[10] G. Herranz, F. Sánchez, N. Dix, D. Hrabovsky, I. C. Infante, J. Fontcuberta, M. V. García-Cuenca, C. Ferrater, and M. Varela, Controlled magnetic anisotropy of $SrRuO_3$ thin films grown on nominally exact $SrTiO_3$(001) substrates, Appl. Phys. Lett. **89**, 152501 (2006).

[11] Y. J. Chang, C. H. Kim, S.-H. Phark, Y. S. Kim, J. Yu, and T. W. Noh, Fundamental thickness limit of itinerant ferromagnetic $SrRuO_3$ thin films, Phys. Rev. Lett. **103**, 057201 (2009).

[12] M. Ziese, I. Vrejoiu, and D. Hesse, Structural symmetry and magnetocrystalline anisotropy of $SrRuO_3$ films on $SrTiO_3$, Phys. Rev. B **81**, 184418 (2010).

[13] D. Kan, R. Aso, H. Kurata, and Y. Shimakawa, Epitaxial strain effect in tetragonal $SrRuO_3$ thin films, J. Appl. Phys. **113**, 173912 (2013).

[14] H. Boschker *et al.*, Ferromagnetism and conductivity in atomically thin $SrRuO_3$, Phys. Rev. X **9**, 011027 (2019).

[15] B. Sohn *et al.*, Sign-tunable anomalous Hall effect induced by two-dimensional symmetry-protected nodal structures in ferromagnetic perovskite thin films, Nat. Mater. **20**, 1643 (2021).

[16] G. Q. Gong, A. Gupta, G. Xiao, P. Lecoeur, and T. R. McGuire, Perovskite oxide superlattices: Magnetotransport and magnetic properties, Phys. Rev. B **54**, R3742 (1996).

[17] L. Qu *et al.*, Asymmetric interfaces and high-T_C ferromagnetic phase in $La_{0.67}Ca_{0.33}MnO_3/SrRuO_3$ superlattices, Nano Res. **14**, 3621 (2021).

[18] P. Padhan, W. Prellier, and R. C. Budhani, Antiferromagnetic coupling and enhanced magnetization in all-ferromagnetic superlattices, Appl. Phys. Lett. **88**, 192509 (2006).

[19] Y. Lee, B. Caes, and B. N. Harmon, Role of oxygen 2p states for antiferromagnetic interfacial coupling and positive exchange bias of ferromagnetic LSMO/SRO bilayers, J. Alloys Compd. **450**, 1 (2008).

[20] J. W. Seo *et al.*, Tunable magnetic interaction at the atomic scale in oxide heterostructures, Phys. Rev. Lett. **105**, 167206 (2010).

[21] M. Ziese *et al.*, Tailoring magnetic interlayer coupling in $La_{0.7}Sr_{0.3}MnO_3/SrRuO_3$ superlattices, Phys. Rev. Lett. **104**, 167203 (2010).

[22] M. Ziese, I. Vrejoiu, E. Pippel, E. Nikulina, and D. Hesse, Magnetic properties of $Pr_{0.7}Ca_{0.3}MnO_3/SrRuO_3$ superlattices, Appl. Phys. Lett. **98**, 132504 (2011).

[23] J. B. Goodenough, An interpretation of the magnetic properties of the perovskite-type mixed crystals $La_{1-x}Sr_xCoO_{3-\lambda}$, J. Phys. Chem. Solids **6**, 287 (1958).

[24] J. Kanamori, Theory of the magnetic properties of ferrous and cobaltous oxides. I, Prog. Theor. Phys. **17**, 177 (1957).

[25] S. Das *et al.*, Low-field switching of noncollinear spin texture at $La_{0.7}Sr_{0.3}MnO_3 - SrRuO_3$ interfaces, Phys. Rev. B **99**, 024416 (2019).

[26] H. Chou, S. G. Hsu, C. B. Lin, and C. B. Wu, Interdiffusion effect on strained $La_{0.8}Ba_{0.2}MnO_3$ thin films by off-axis sputtering on $SrTiO_3$ (100) substrates, Appl. Phys. Lett. **90**, 062501 (2007).

[27] S. Martín-Rio, Z. Konstantinović, A. Pomar, Ll. Balcells, J. Pablo-Navarro, M. R. Ibarra, C. Magén, N. Mestres, C. Frontera, and B. Martínez, Spin-to-charge conversion in all-oxide $La_{2/3}Sr_{1/3}MnO_3/SrIrO_3$ heterostructures, ACS Appl. Mater. Interfaces **15**, 37038 (2023).

[28] F. Stramaglia, G. Panchal, F. Nolting, and C. A. F. Vaz, Role of interdiffusion on the magnetism of ultrathin $LaMnO_3$ films, AIP Adv. **14**, 025021 (2024).

[29] D. Howe, Z. Wang, M. Saghayezhian, Z. Ali, P. Siwakoti, H. Ling, Y. Liang, E. W. Plummer, Y. Zhu, and J. Zhang, Buffer-layer effect on the ferromagnetism of manganite heterojunctions, Phys. Rev. Mater. **9**, 044409 (2025).

[30] See Supplemental Material at http://link.aps.org/supplemental/10.1103/mxfx-fg4f for additional structural, magnetic, and spectroscopic data, STO-spacer control experiments, and computational details and additional results of the first-principles calculations, which also includes Refs. [48–56].

[31] K. Michaeli, A. C. Potter, and P. A. Lee, Superconducting and ferromagnetic phases in $SrTiO_3/LaAlO_3$ oxide interface structures: Possibility of finite momentum pairing, Phys. Rev. Lett. **108**, 117003 (2012).

[32] M. Basletić, J.-L. Maurice, C. Carrétéro, G. Herranz, O. Copie, M. Bibes, É. Jacquet, K. Bouzehouane, S. Fusil, and

A. Barthélémy, Mapping the spatial distribution of charge carriers in $LaAlO_3/SrTiO_3$ heterostructures, Nat. Mater. **7**, 621 (2008).

[33] A. D. Caviglia, S. Gariglio, N. Reyren, D. Jaccard, T. Schneider, M. Gabay, S. Thiel, G. Hammerl, J. Mannhart, and J.-M. Triscone, Electric field control of the $LaAlO_3/SrTiO_3$ interface ground state, Nature (London) **456**, 624 (2008).

[34] M. P. Warusawithana *et al.*, $LaAlO_3$ stoichiometry is key to electron liquid formation at $LaAlO_3/SrTiO_3$ interfaces, Nat. Commun. **4**, 2351 (2013).

[35] G. Singh-Bhalla, C. Bell, J. Ravichandran, W. Siemons, Y. Hikita, S. Salahuddin, A. F. Hebard, H. Y. Hwang, and R. Ramesh, Built-in and induced polarization across $LaAlO_3/SrTiO_3$ heterojunctions, Nat. Phys. **7**, 80 (2011).

[36] A. P. Ramirez, Colossal magnetoresistance, J. Phys.: Condens. Matter **9**, 8171 (1997).

[37] T. Hashimoto, S. Ishibashi, and K. Terakura, Jahn-Teller distortion and magnetic structure in $LaMnO_3$: A first-principles theoretical study with full structure optimizations, Phys. Rev. B **82**, 045124 (2010).

[38] G. Koster, L. Klein, W. Siemons, G. Rijnders, J. S. Dodge, C.-B. Eom, D. H. A. Blank, and M. R. Beasley, Structure, physical properties, and applications of $SrRuO_3$ thin films, Rev. Mod. Phys. **84**, 253 (2012).

[39] A. Tebano *et al.*, Evidence of orbital reconstruction at interfaces in ultrathin $La_{0.67}Sr_{0.33}MnO_3$ films, Phys. Rev. Lett. **100**, 137401 (2008).

[40] J. Xia, W. Siemons, G. Koster, M. R. Beasley, and A. Kapitulnik, Critical thickness for itinerant ferromagnetism in ultrathin films of $SrRuO_3$, Phys. Rev. B **79**, 140407(R) (2009).

[41] R. Peng, H. C. Xu, M. Xia, J. F. Zhao, X. Xie, D. F. Xu, B. P. Xie, and D. L. Feng, Tuning the dead-layer behavior of $La_{0.67}Sr_{0.33}MnO_3/SrTiO_3$ via interfacial engineering, Appl. Phys. Lett. **104**, 081606 (2014).

[42] A. Vailionis, H. Boschker, Z. Liao, J. R. A. Smit, G. Rijnders, M. Huijben, and G. Koster, Symmetry and lattice mismatch induced strain accommodation near and away from correlated perovskite interfaces, Appl. Phys. Lett. **105**, 131906 (2014).

[43] Z. Ali, Z. Wang, A. O'Hara, M. Saghayezhian, D. Shin, Y. Zhu, S. T. Pantelides, and J. Zhang, Origin of insulating and nonferromagnetic $SrRuO_3$ monolayers, Phys. Rev. B **105**, 054429 (2022).

[44] I. Khomskii, *Transition Metal Compounds* (Cambridge University Press, Cambridge, UK, 2014).

[45] J. Chakhalian, J. W. Freeland, H.-U. Habermeier, G. Cristiani, G. Khaliullin, M. van Veenendaal, and B. Keimer, Orbital reconstruction and covalent bonding at an oxide interface, Science **318**, 1114 (2007).

[46] P. Yu *et al.*, Interface ferromagnetism and orbital reconstruction in $BiFeO_3-La_{0.7}Sr_{0.3}MnO_3$ heterostructures, Phys. Rev. Lett. **105**, 027201 (2010).

[47] A. Zakharova, M. Caputo, E. B. Guedes, M. Radovic, F. Nolting, and C. Piamonteze, Interplay between magnetism and interface-induced effects in ultrathin manganites, Phys. Rev. Mater. **5**, 124404 (2021).

[48] P. Hohenberg and W. Kohn, Inhomogeneous electron gas, Phys. Rev. **136**, B864 (1964).

[49] W. Kohn and L. J. Sham, Self-consistent equations including exchange and correlation effects, Phys. Rev. **140**, A1133 (1965).

[50] G. Kresse and J. Furthmüller, Efficient iterative schemes for *ab initio* total-energy calculations using a plane-wave basis set, Phys. Rev. B **54**, 11169 (1996).

[51] J. P. Perdew, K. Burke, and M. Ernzerhof, Generalized gradient approximation made simple, Phys. Rev. Lett. **77**, 3865 (1996).

[52] J. B. A. A. Elemans, B. van Laar, K. R. van der Veen, and B. O. Loopstra, The crystallographic and magnetic structures of $La_{1-x}BaxMn_{1-x}MexO_3$ (Me = Mn or Ti), J. Solid State Chem. **3**, 238 (1971).

[53] I. Koriba, B. Lagoun, A. Guibadj, S. Belhadj, A. Ameur, and A. Cheriet, Structural, electronic, magnetic and mechanical properties of three $LaMnO_3$ phases: Theoretical investigations, Comput. Condens. Matter **29**, e00592 (2021).

[54] J. M. Rondinelli, N. M. Caffrey, S. Sanvito, and N. A. Spaldin, Electronic properties of bulk and thin film $SrRuO_3$: Search for the metal-insulator transition, Phys. Rev. B **78**, 155107 (2008).

[55] J. H. Haeni *et al.*, Room-temperature ferroelectricity in strained $SrTiO_3$, Nature (London) **430**, 758 (2004).

[56] H. J. Monkhorst and J. D. Pack, Special points for Brillouin-zone integrations, Phys. Rev. B **13**, 5188 (1976).